Micro-Supercapacitors Based on Interdigital Electrodes of Reduced Graphene Oxide and Carbon Nanotube Composites with Ultrahigh Power Handling Performance

*Majid Beidaghi and Chunlei Wang**

A novel method for fabricating micro-patterned interdigitated electrodes based on reduced graphene oxide (rGO) and carbon nanotube (CNT) composites for ultra-high power handling micro-supercapacitor application is reported. The binder-free microelectrodes were developed by combining electrostatic spray deposition (ESD) and photolithography lift-off methods. Without typically used thermal or chemical reduction, GO sheets are readily reduced to rGO during the ESD deposition. Electrochemical measurements show that the in-plane interdigital design of the microelectrodes is effective in increasing accessibility of electrolyte ions in-between stacked rGO sheets through an electro-activation process. Addition of CNTs results in reduced restacking of rGO sheets and improved energy and power density. Cyclic voltammetry (CV) measurements show that the specific capacitance of the micro-supercapacitor based on rGO–CNT composites is 6.1 mF cm^{-2} at 0.01 V s^{-1}. At a very high scan rate of 50 V s^{-1}, a specific capacitance of 2.8 mF cm^{-2} (stack capacitance of 3.1 F cm^{-3}) is recorded, which is an unprecedented performance for supercapacitors. The addition of CNT, electrolyte-accessible and binder-free microelectrodes, as well as an interdigitated in-plane design result in a high-frequency response of the micro-supercapacitors with resistive-capacitive time constants as low as 4.8 ms. These characteristics suggest that interdigitated rGO–CNT composite electrodes are promising for on-chip energy storage application with high power demands.

1. Introduction

Recent development in miniaturized electronic devices has increased the demand for power sources that are sufficiently compact and can potentially be integrated on a chip with other electronic components. Miniaturized electrochemical capacitors (EC) or micro-supercapacitors have great potential to complement or replace batteries and electrolytic capacitors in a variety of applications.[1–10] Among all the desired properties of a micro-supercapacitor device, high power density and more importantly high frequency response and rate capability are crucial for their future applications. These properties are particularly important if the micro-supercapacitors were to be coupled with micro-batteries, micro-fuel cells, and energy harvesters to provide peak power; or if they were to replace electrolytic capacitors in applications such as filtering voltage ripples in line-powered electronics (ac line-filtering).[11] Achieving a high frequency response and rate capability is dependent on the various constituents of a supercapacitor including the electrode materials, the electrolyte, the method of assembly of materials on the current collectors, and the architecture of the device.

ECs are categorized into two types based on their energy storage mechanism, electrical double-layer capacitors (EDLCs) and pseudo-capacitors. EDLCs store charge by adsorption of electrolyte ions on the surface of an electrode with high specific surface area. Different types of high surface area carbon materials are usually used as electrode materials for EDLCs. Pseudo-capacitors store charge by faradic reactions that takes place on the surface or sub-surface of the electrodes. Metal oxides such as Ruthenium oxide,[2] Manganese oxide,[3] and Vanadium oxide[4] conducting polymers such as Polypyrrole (PPy)[5] and Polyaniline (PANI)[6] are reported as pseudo-capacitive materials for micro-supercapacitors. Although pseudo-capacitive materials show promising volumetric capacitance, the slow charge storage mechanism immensely impacts their frequency response and rate handling capabilities. Carbon nanomaterial such as, activated carbon (AC),[7] carbide derived carbon (CDC),[8,9] onion-like carbon (OLC),[10] carbon nanotube (CNT),[11] and graphene[12] have been used to fabricate EDLC micro-supercapacitors. Micro-supercapacitors based on AC show medium stack capacitance, however due to the use of polymeric binders and limited ion transfer in the porous network of the electrode materials, AC micro-supercapacitors show a relatively poor frequency response.[7] The CDC based micro-supercapacitors show high volumetric capacitance at low scan rates (about 180 Fcm^{-3} volumetric capacitance of one electrode at 20 mVs^{-1}), however the capacitance drops to almost half of its initial value by increasing the scan rate to 500 mVs^{-1}, suggesting the poor rate handling capability of these micro-supercapacitors.[9] Among all the reported EDLC micro-supercapacitors, those based on OLCs are particularly notable as they offer ultra-high power handling capability

M. Beidaghi, Prof. C. Wang
Department of Mechanical and Materials Engineering
Florida International University
10555 W. Flagler St., EC 3463, FL 33174, USA
E-mail: wangc@fiu.edu

DOI: 10.1002/adfm.201201292

with a resistance capacitance (RC) time constant of only 26 ms.[10] The combination of micrometer-sized interdigital electrode design with a binder free deposition technique and the non-porous morphology of OLC materials was responsible for the excellent frequency response of OLC based micro-supercapacitors. The drawback of OLC based micro-supercapacitors is their modest specific capacitance (1.7 $mFcm^{-2}$) and their high temperature processing requirements (~1800 °C).[10]

Graphene has recently become a material of interest in supercapacitor application due to its high theoretical surface area and electrical conductivity.[13–17] Miller and coworkers[13] demonstrated that vertically oriented graphene grown on nickel foam has excellent frequency response with an RC time constant of less than 0.2 ms. However, this was achieved at the cost of low specific capacitance resulting from the low density of electrode materials.[13] Sheng et al.[14] reported a very similar frequency response with an RC time constant of about 0.23 ms for interpenetrating graphene electrodes prepared by electrochemical reduction of graphene oxide. However, this performance was also achieved for electrodes with a very low mass density, resulting in a maximum capacitance of only 0.325 $mFcm^{-2}$ at a low frequency of 1 Hz.[14] The performance of graphene-based supercapacitor materials is usually hindered by the fact that graphene sheets tend to aggregate and restack during processing and the actual accessible surface area of the electrodes is much lower compared to the theoretical surface area (more than 2600 m^2g^{-1}). One of the effective strategies to avoid this problem is the addition of spacers such as carbon nanotubes (CNTs) between graphene sheets to prevent their restacking.[18–20] Another interesting approach to increase the accessibility of electrolyte ions to graphene sheets is the approach reported by Yoo and coworkers[21] where the in-plane design of the two supercapacitor electrodes resulted in a dramatic increase in capacitance compared to the conventional 2D stacking of the electrodes. The authors suggested that the in-plane design will increase the accessibility of ions to the surface of the graphene sheets and thus improve the capacitive properties.[21] It can be anticipated that the efficiency of the in-plane design of the electrode can be increased if the electrodes were made in micro meter scale sizes. There have been some efforts to utilize graphene as an electrode material for micro-supercapacitors. Gao et al.[12] reported a direct write process to fabricate micro-supercapacitors with interdigital electrode design and hydrated graphene oxide (GO) as the electrolyte and separator. While this fabrication method is promising, the electrodes demonstrated in this work was fabricated in millimeter scales with the maximum capacitance of only 0.51 $mFcm^{-2}$ for an in-plane design of electrodes. It remains a challenge to develop micron-size patterned graphene electrodes through a scalable and reliable fabrication method.

In this work we report on ultra-high power micro-supercapacitors based on binder-free reduced graphene oxide (rGO) and rGO/CNT hybrid as electrode materials. The micro-supercapacitors with interdigital microelectrodes (100 μm width and 50 μm spacing) are readily fabricated through the combination of electrostatic spray deposition (ESD) and photolithography lift-off. We first demonstrate that ESD can be used for simultaneous deposition and reduction of GO. Next, in order to maximize the accessibility of electrolyte ions to electrode materials, we demonstrate the effects of the addition of CNTs between rGO sheets when integrated in micron-sized in-plane electrodes. The electrochemical properties of micro-supercapacitors were examined by cyclic voltammetry (CV), galvanostatic charge-discharge (CD), and electrochemical impedance spectroscopy (EIS). The micro-supercapacitors show exceptionally high rate capability and power handling performance and can be charged and discharged at a CV scan rate of 50 Vs^{-1} and a CD rate of 100 $mAcm^{-2}$ (~450–600 Ag^{-1}). These rates are about three orders of magnitude higher than the charge and discharge rates of conventional supercapacitors. EIS measurements show a very high frequency response of micro-supercapacitors with characteristic frequencies as high as 290.76 Hz, higher than the recently reported state of the art micro-supercapacitors.

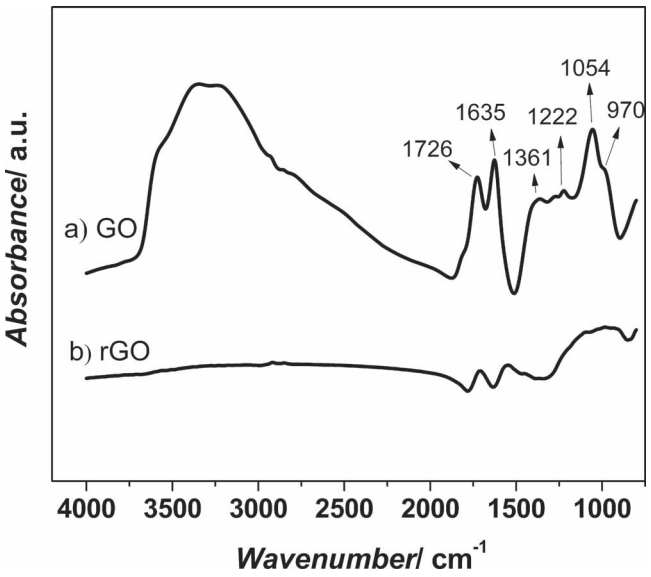

Figure 1. FTIR absorbance spectra of: a) as-purchased GO powder, and b) ESD deposited rGO.

2. Results and Discussion

A homogeneous and stable solution of GO in 1,2 propanediol was used as the precursor solution for ESD deposition of GO on preheated (250 °C) substrates. The studies of the surface chemistry of deposited films with Fourier Transform Infrared Spectroscopy (FTIR) and X-ray photoelectron spectroscopy (XPS) show that the GO reduced to rGO during the deposition. The FTIR Spectra of GO before and after deposition are shown in **Figure 1**. The broad adsorption peak centering at around 3300 cm^{-1} in the spectrum of GO is assigned as isolated hydroxyl groups and water, which also signals an H-O-H bending at 1635 cm^{-1}.[22,23] The peak at 1054 cm^{-1} is consistent with C-O stretching vibration. The presence of phenol and carboxylic acid groups was signaled by the phenolic C-O peak at 1222 cm^{-1} and the mode at 1726 cm^{-1} which is assigned to C = O stretching vibrations from carbonyl and carboxylic groups. Based on the structural model of GO, these groups are placed on the periphery of GO sheets.[23,24] The spectrum also shows

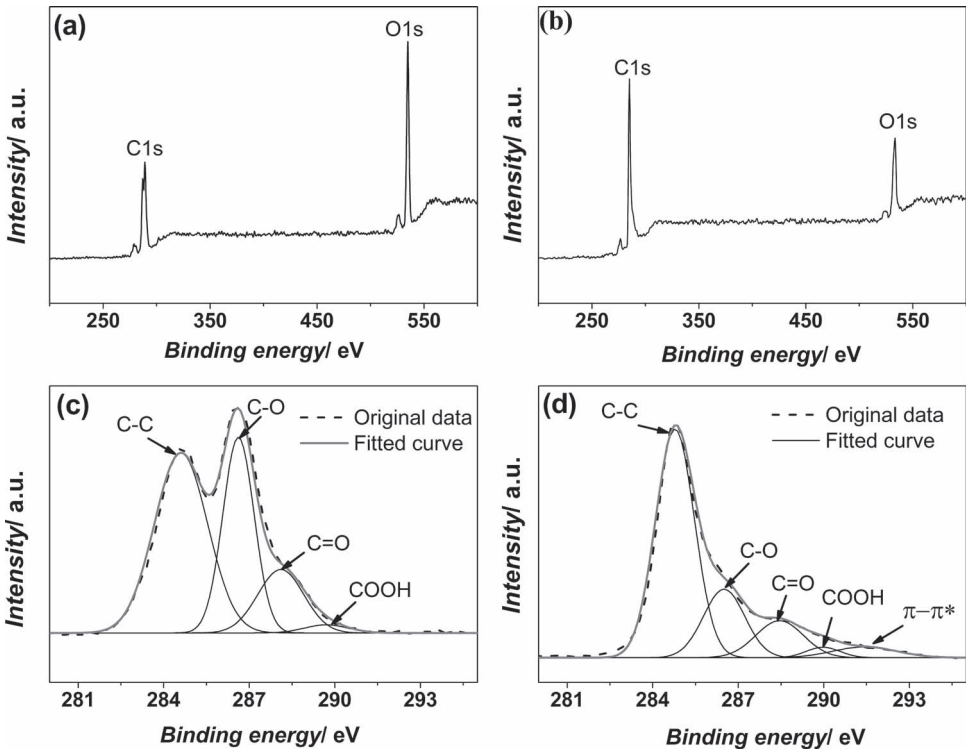

Figure 2. Wide-range XPS spectra of: a) GO, and b) rGO. The C1s spectra were deconvoluted into their corresponding components using a Gaussian function for c) GO, and d) rGO.

the presence of epoxy C-O (970 cm^{-1}) and O-H bending in tertiary alcohol (1361 cm^{-1}) groups which are reported to be located on the basal plane of GO.[23,24] After the deposition, the intensities of modes from water and oxygen functionalities were significantly reduced. The FTIR spectrum of deposited rGO shows mainly bands originating from C-O stretching, phenolic C-O stretching and C=O stretching while the signals from tertiary alcohol and epoxy C-O on the basal plane of GO disappeared after deposition. The FTIR analysis suggests that the remaining oxygen groups after reduction are the functional groups that are mainly attached to the periphery of rGO sheets.[23,24]

The surface chemistry of GO and the as-deposited rGO were studied by X-ray photoelectron spectroscopy (XPS). The XPS spectra of GO and rGO are shown in **Figure 2**a,b. The O1s peak intensity has decreased for deposited rGO and the overall C/O ratio has increased to 5.75 compared to 1.77 for the GO powder. This seemingly mediocre increase in C/O ratio represents a large decrease in oxygen content (~70%) on the surface rGO sheets. The C1s spectrum of GO can be deconvoluted to four components corresponding to four types of carbon bonds within GO. The peaks centered at 284.6, 286.6, 288.1 and 289.7 eV, correspond to C-C in aromatic rings, C-O (epoxy and alkoxy), C = O (carbonyl and carboxylic) and COOH groups, respectively.[22–24] The C1s spectrum of rGO shows all these four peaks with different proportions. The proportion of C-C bond has increased from 50% for GO to about 61% for deposited rGO. The proportion of the peak corresponding to C-O groups (286.6 eV) has decreased after the deposition. The proportion of C-O groups is 32% for GO and about 19% for the rGO. The remaining C-O groups should correspond to peripheral phenolic and carboxyl functionalities. The proportion of the C = O groups shows a slight decrease after deposition, from 15% for GO to 12% for rGO. In addition to these four peaks, a π–π* shake up satellite peak was observed for rGO at around 291.4 eV. This is a characteristic of aromatic or conjugated systems which indicates that there are less defects in the structure of rGO after the deposition.[25,26] The XPS results confirm the FTIR results and show the reduction of GO after the ESD deposition. This is in agreement with previous studies regarding the reduction of GO at low temperatures (150–250 °C) in air or in organic solvents.[22,27] The remaining oxygen content after the reduction should correspond to phenolic, carbonyl, and carboxyl groups in the periphery of deposited rGO sheets.[23] The reduction of GO after ESD deposition was also confirmed by electrical conductivity measurements where conducitvity was increased from $<10^{-3}$ Sm^{-1} for GO to about 93 Sm^{-1} for ESD deposited rGO samples.

Figure 3a schematically shows the procedure used to integrate electrode materials on interdigital Ti/Au microelectrodes to fabricate micro-supercapacitors. Before the ESD deposition, the working area of the microelectrodes was defined by a removable microfabricated photoresist mask that covers the contact pads and the space between the microelectrodes. After the deposition and removal of the mask, a micro-supercapacitor with 20 in-plane interdigital microelectrodes (10 positive and 10 negative microelectrodes) was constructed. Each microelectrode was 100 μm in width and 2500 μm in length and the distance between adjacent microelectrodes were 50 μm. The samples

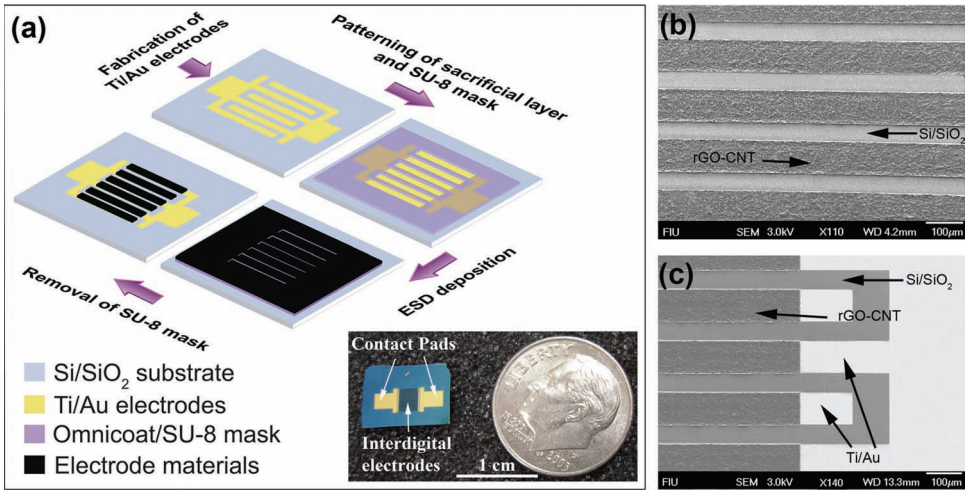

Figure 3. a) Schematic drawing of fabrication procedures of micro-supercapacitors (inset shows a digital photograph of a fabricated device). b,c) Top view SEM images of rGO–CNT-based interdigital microelectrode arrays.

labeled as rGO and CNT were fabricated from the deposition solution containing 100% GO and 100% CNT, respectively. The samples labeled as rGO-CNT-9-1 and rGO-CNT-8-2 had GO:CNT weight ratios of 9:1 and 8:2, respectively. The thicknesses of all electrodes were kept around 6 μm by adjusting the deposition rate for each type of electrode materials. Figure 3b,c show the scanning electron microscopy (SEM) images of a typical fabricated micro-supercapacitor. The microelectrodes had well-defined and defect-free patterns and no short circuits between the electrodes were detected.

The microstructure of deposited rGO microelectrodes (**Figure 4**a) showed stacked layers of graphene sheets with micron-sized wrinkles that are probably the result of GO sheets bending during the deposition. Figure 4b, a tilted view from the side of an interdigital electrode, shows the local folding and non-uniform stacking of the rGO layers. Several to hundreds of stacked graphene sheets can be observed locally with extended irregular porous structures, which could act as diffusion channels and facilitate easy penetration of ions in the bulk of the microelectrodes. However, heavily stacked rGO sheets could prevent the full access of electrolyte ions to the surface rGO sheets. Figures 4c-f show the SEM images of rGO–CNT hybrid electrodes. The tilted view SEM images clearly show uniformly packed film with the appearance of CNTs between the rGO sheets throughout the thickness of deposited films with almost no sign of stacked rGO sheets.

In order to study the electrochemical performance of fabricated micro-supercapacitors, CV was conducted in 3 M KCl aqueous electrolyte and at the potential range of 0 to 1 V. During the initial CV cycles of the rGO micro-supercapacitor at a 0.1 Vs^{-1} scan rate, the CV current during cycling constantly increased up to 200 cycles, with the average current density increasing by more than 7 times compared to the first cycle (**Figure 5**a). After about 200 cycles the rate of the increase in average current dropped and for the following cycles up to the 1000^{th} cycle, an increase of less than 5% in current density was noted (Figure 5a,b). A similar phenomenon has been reported by Cheng et al. during long time cycling of graphene electrodes and was referred to as "electro-activation".[18] The authors detected a 60% increase in specific capacitance of pristine graphene electrodes during longtime cycling. It was suggested that the intercalation of electrolyte ions between the graphene sheets increases the spacing between the sheets and therefore increases the accessibility of ions to the surface of graphene. It should be noted that the effect of electro-activation is much more pronounced in the case of the interdigital rGO electrodes compared to the planar electrodes reported by Cheng and coworkers.[18] In general, the in-plane design of the graphene electrodes increases the accessibility of ions in between graphene sheets.[21] In the case of rGO micro-supercapacitors, in addition to the side by side design of the electrodes, the smaller size of the electrodes and the shorter distance between them further facilitate the accessibility of ions to the graphene sheets, resulting in a more efficient electro-activation. In contrast to the rGO microdevice, the average CV current density of rGO–CNT micro-supercapacitors did not increase during the cyclic test for 1000 cycles showing that the electro-activation did not occur in the case of these microdevices (Figure 5b). This observation leads us to conclude that the addition of CNTs had effectively prevented the restacking of rGO sheets and thus the intercalation of ions during cycling could not further increase the spacing between the rGO sheets. Furthermore, the microdevices with hybrid rGO–CNT electrodes show higher CV current densities, implying that compared to electro-activation, using CNTs as a spacer between graphene sheets is a more effective way to increase the accessible surface area of the electrodes.

The rate capability and power handling of the micro-supercapacitors was tested by CV at very high scan rates (1 to 50 Vs^{-1}). Before performing the tests at higher scan rates, each microdevice was cycled for 250 cycles at 0.1 Vs^{-1} to ensure that the CVs were stable and in the case of the rGO microdevices the electro-activation was completed. **Figure 6**a–e show the CV curves of rGO, rGO-CNT-9-1 and rGO-CNT-8-2 microdevices at different scan rates. The rGO micro-supercapacitor showed

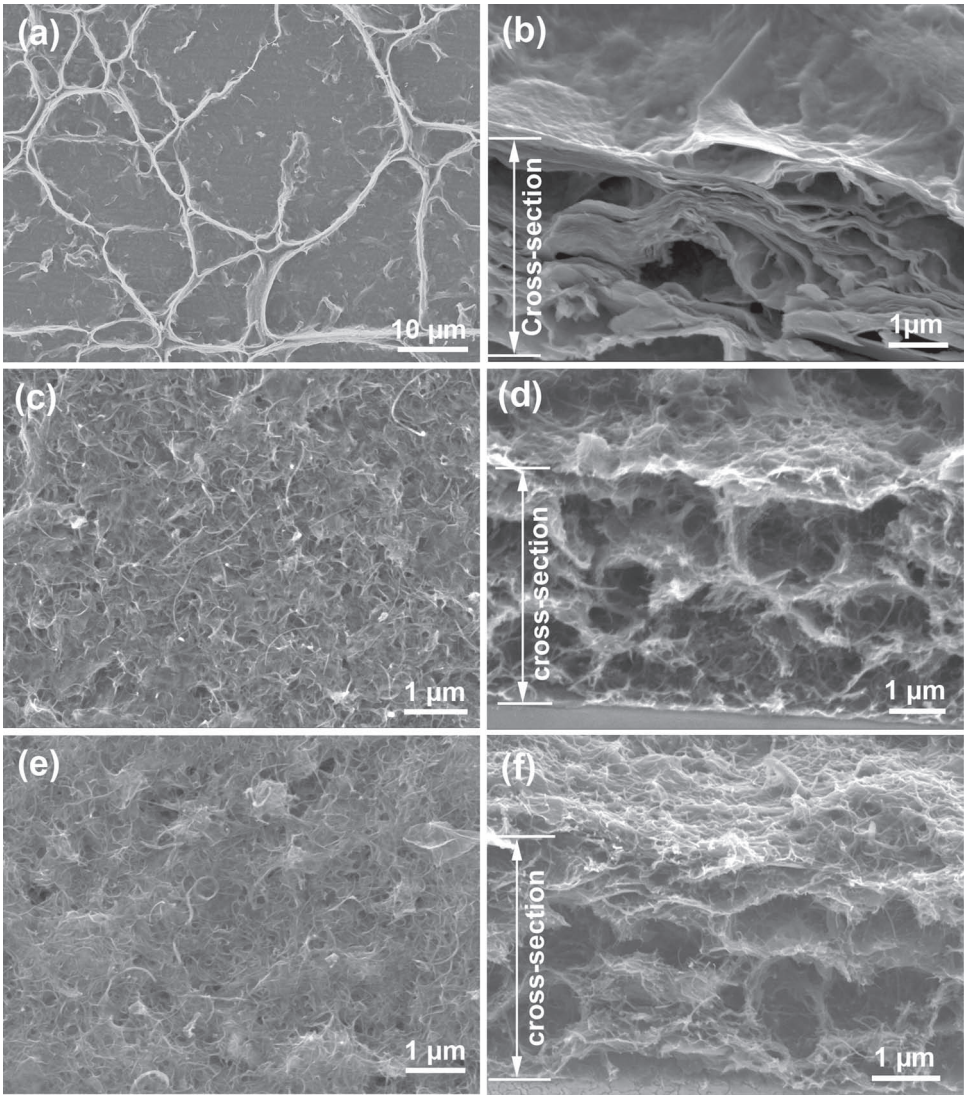

Figure 4. Scanning electron images showing the morphology of the deposited electrodes. Top view and tilted 35° view, respectively of: a,b) rGO microelectrodes; c,d) rGO-CNT-9-1 microelectrodes; e,f) rGO-CNT-8-2 microelectrodes.

near rectangular CV curves, which is typical of EDLCs, at scan rates of 1 and 5 Vs^{-1}. Upon increasing the scan rate to 10 Vs^{-1}, the CV curve deviated from a rectangular shape which indicates a more resistive behavior. At much higher scan rates of 25 and 50 Vs^{-1}, the rGO microdevice still showed some capacitive behavior, but the resistive behavior was dominant and the capacitance dropped quickly at these scan rates. In the case of microdevices with rGO–CNT electrodes, the CV curve showed a rectangular shape with pure capacitive behavior even at a very high scan rate of 50 Vs^{-1}.

The stack capacitance (volumetric capacitance) of the micro-supercapacitors were calculated from the CV curves at various scan rates and by taking into account the volume of both electrodes and the space between them (Figure 6f). As suggested by Gogotsi and Simon,[28] the volumetric or areal capacitance or energy density are much more reliable performance metrics for supercapacitor devices compared to gravimetric capacitance. This is more pronounced in the case of microdevices as the weight of the material of a thin film electrode on a chip is negligible.[28] As it is evident from Figure 6e, all micro-supercapacitors with different compositions showed capacitive behavior even at a very high scan rate of 50 Vs^{-1}. However, the rGO–CNT micro-supercapacitors showed better performance in terms of capacitance and rate capability. The rGO micro-supercapacitor showed a stack capacitance of about 4.4 Fcm^{-3} (~27.2 Fcm^{-3} volumetric capacitance of one electrode) at a scan rate of 0.01 Vs^{-1} which dropped to 3.2 Fcm^{-3} at a 1 Vs^{-1} scan rate. At a higher scan rate of 50 Vs^{-1}, the stack capacitance decreased to 0.7 Fcm^{-3} (~4.4 Fcm^{-3} volumetric capacitance of one electrode). This value at a 50 Vs^{-1} scan rate is about 16% of the initial stack capacitance recorded at a 0.01 Vs^{-1} scan rate. The rGO-CNT-9-1 micro-supercapacitor showed the highest stack capacitance at

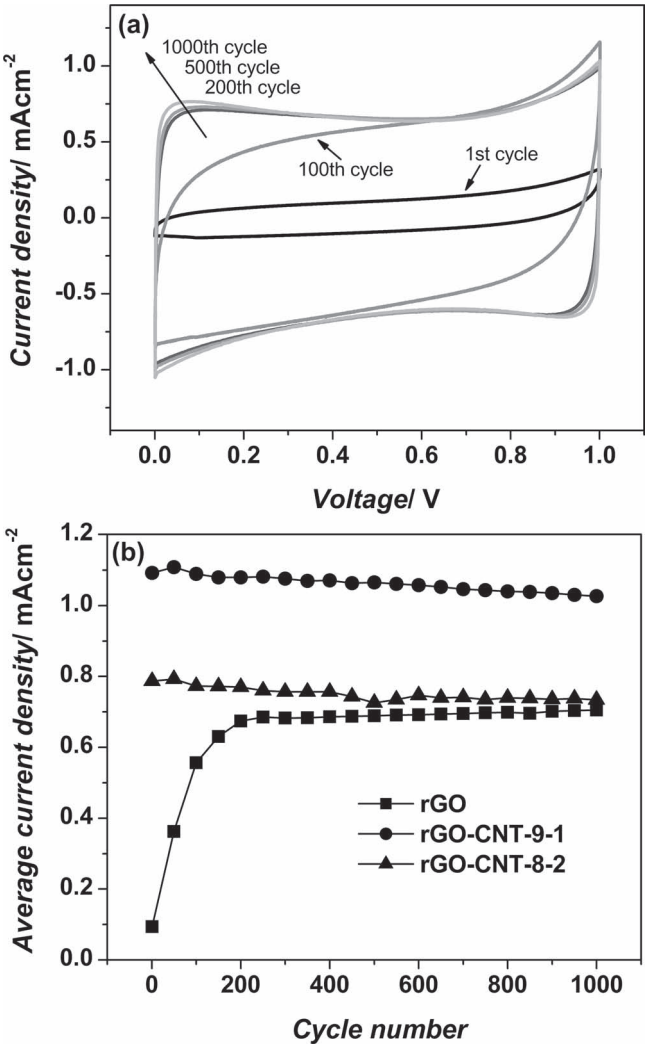

Figure 5. a) CV curves at various cycles of a rGO micro-supercapacitors tested at 0.1 Vs^{-1} scan rate. b) Variation of average CV current density with cycle number for rGO, rGO-CNT-9-1, and rGO-CNT-8-2.

all CV scan rates. At the low scan rate of 0.01 Vs^{-1}, the stack capacitance was about 6.1 Fcm^{-3} which is equivalent to 37.5 Fcm^{-3} volumetric capacitance of one electrode. When the scan rate was increased to 1 Vs^{-1} the stack capacitance dropped to about 5.0 Fcm^{-3}. At the scan rate of 50 Vs^{-1} the stack capacitance was about 3.1 Fcm^{-3} which is 50% of its value at the 0.01 Vs^{-1} scan rate and 62% percent of its value at the 1 Vs^{-1} scan rate. The rGO-CNT-8-2 micro-supercapacitor showed a stack capacitance of about 2.4 Fcm^{-3} at a scan rate of 50 Vs^{-1} which is 46% of the capacitance at a 0.01 Vs^{-1} scan rate (5.2 Fcm^{-3}) and 70% of the capacitance at the scan rate of 1 Vs^{-1} (3.4 Fcm^{-3}). The lower capacitance of rGO-CNT-8-2 micro-supercapacitors could be explained by the effect of additional CNT which has lower capacitance compared to rGO sheets (Figure 6f). However, the lower drop in stack capacitance of rGO-CNT-8-2 micro-supercapacitors (30%) compared to the rGO-CNT-9-1 micro-supercapacitor (38%) upon increasing the scan rate from 1 to 50 Vs^{-1} indicates that additional CNT has improved the rate capability of the microdevice. The micro-supercapacitor based on 100% CNT shows much lower capacitance compared to rGO and rGO–CNT micro-supercapacitors at all scan rates (Figure 6f). The areal specific capacitance of the rGO-CNT-9-1 microdevice (calculated by taking into account the total area of both electrodes) is about 2.8 $mFcm^{-2}$ at a 50 Vs^{-1} scan rate. The significance of the electrochemical properties of the rGO–CNT micro-supercapacitors can be further revealed when they are compared to the performance of other reported micro-supercapacitors. Even at a high scan rate of 50 Vs^{-1} the rGO–CNT micro-supercapacitors showed higher specific capacitance compared to the majority of reported EDLC micro-supercapacitors (specific capacitance of 0.4-2 $mFcm^{-2}$ at very low CV scan rates of 0.01 to 0.1 Vs^{-1}).[7,11,12,29] Some other reported EDLC micro-supercapacitors such as graphene-cellulose paper supercapacitors and CDC micro-supercapacitors show higher specific capacitance but poor rate capability and frequency response.[9,30] Finally, the high power OLC based micro-supercapacitors reported by Pech et al.[10] show similar high rate capability but have lower capacitance compared to rGO–CNT micro-supercapacitors. For instance, a stack capacitance of about 0.9 Fcm^{-3} was measured at a 50 Vs^{-1} scan rate for OLC based micro-supercapacitors (please see Table S1 for a more detailed comparison of different EDLC micro-supercapacitors).

The electrochemical performance of micro-supercapacitors was further studied by CD at different current densities and EIS. The CD curves showed triangular shapes, typical of EDLC supercapacitors, with a very low *iR* drop even at a very high current density of 60 $mAcm^{-2}$ (**Figure 7**a). The *iR* drop, the sudden voltage drop at the beginning of the CD discharge, is a measure of the overall resistance of the cell and since its value is proportional to discharge current, the small *iR* drop of the micro-supercapacitors at a high discharge current indicates a very low cell resistance for all the tested micro-supercapacitors. The *iR* drop slightly decreased with an increase in the amount of CNTs in the electrodes and its value was 0.024, 0.013 and 0.010 V for rGO, rGO-CNT-9-1, and rGO-CNT-8-2 micro-supercapacitors, respectively. The areal specific capacitances of the micro-supercapacitors were calculated from CD curves at different discharge current densities and are shown in Figure 7b. The results from CD experiments were in good agreement with the CV results in terms of specific capacitance and rate handling of micro-supercapacitors. The highest specific capacitances at all discharge currents were achieved for the rGO-CNT-9-1 micro-supercapacitor with a specific capacitance of 5.1 $mFcm^{-2}$ at a 3 $mAcm^{-2}$ discharge current density which dropped only by about 30% at a very high current density of 100 $mAcm^{-2}$ (3.6 $mFcm^{-2}$). In comparison, the rGO-CNT-8-2 micro-supercapacitor showed a lower specific capacitance (3.4 $mFcm^{-2}$ at 3 $mAcm^{-2}$ current density), but slightly improved rate handling as its specific capacitance dropped by 26% upon increasing the discharge current to 100 $mAcm^{-2}$. Based on our estimation of the weight of the electrode materials for each micro-supercapacitor (~4.5–6.2 μg), a discharge areal current density of 100 $mAcm^{-2}$ approximately corresponds to gravimetric current density in the range of 450 to 600 Ag^{-1}, which is more than two orders of magnitude higher than the discharge current densities that are usually used in testing supercapacitors.[31]

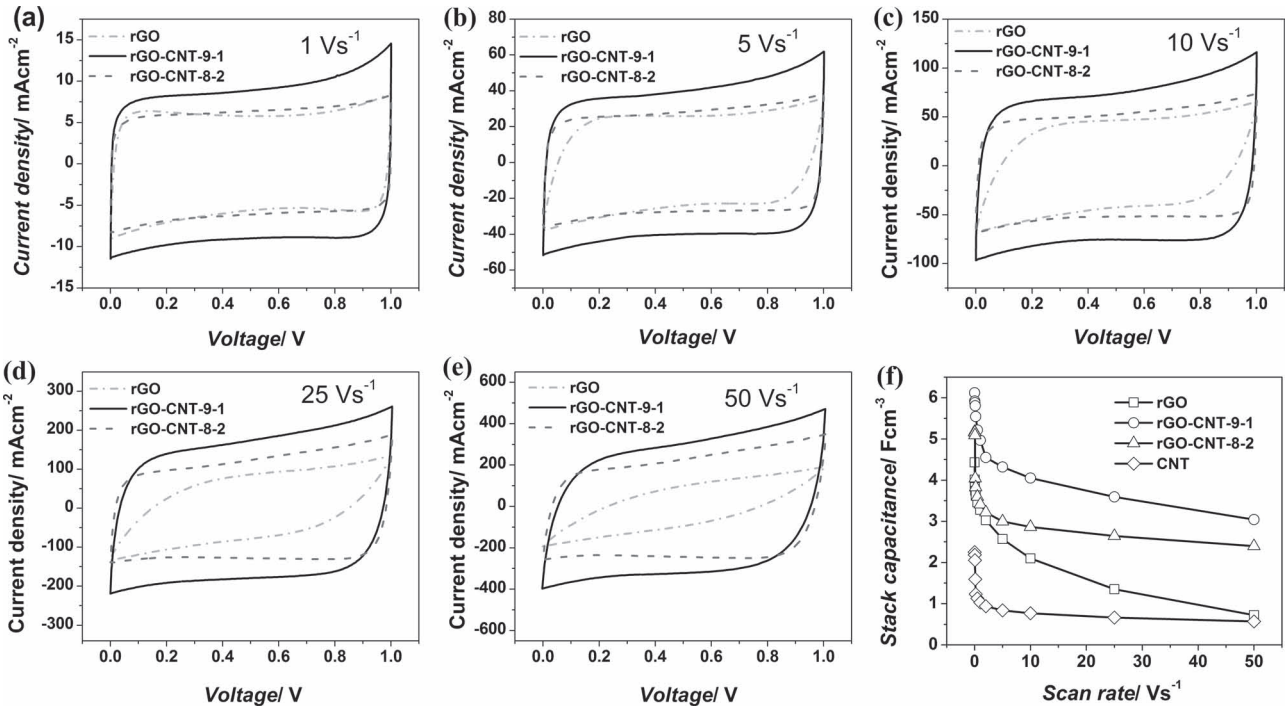

Figure 6. CV curves of rGO, rGO-CNT-9-1, and rGO-CNT-8-2 micro-supercapacitors at scan rates of: a) 1 Vs^{-1}, b) 5 Vs^{-1}, c) 10 Vs^{-1}, d) 25 Vs^{-1}, and e) 50 Vs^{-1}. f) Comparison of stack capacitances of micro-supercapacitors with different electrode compositions.

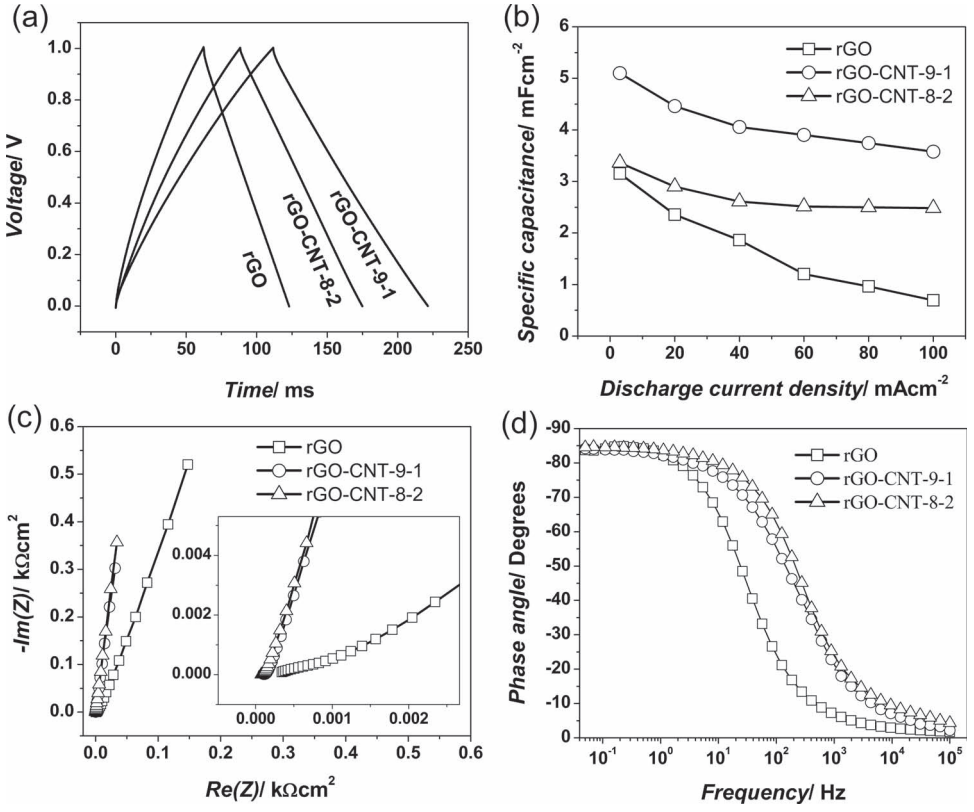

Figure 7. a) Charge-discharge curves of micro-supercapacitors based on rGO, rGO-CNT-9-1, and rGO-CNT-8-2 electrodes. b) Specific capacitances of micro-supercapacitor at different discharge current densities. c) Nyquist plots of different micro-supercapacitors (inset shows the Nyquist plots at higher frequencies). d) Phase angle vs frequency for the different micro-supercapacitors.

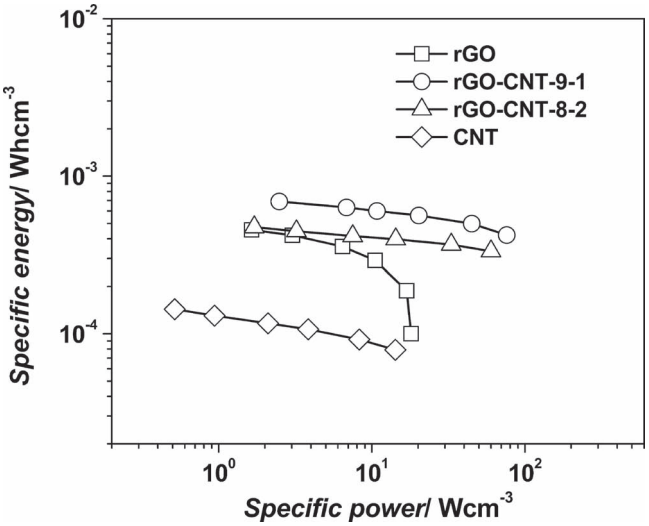

Figure 8. Ragone plot showing the relationship of specific energy and the specific power of micro-supercapacitors.

The frequency response of the micro-supercapacitors was studied by EIS. The Nyquist plots of the micro-supercapacitors show typical features of EDCL supercapacitors (Figure 7c). For an ideal EDLC the low-frequency region of the Nyquist plot is a straight line. The more vertical the line, the more closely the supercapacitor behaves as an ideal capacitor.[15,16,32] The low-frequency regions of Nyquist plots of rGO–CNT hybrid devices show straight lines with an almost 90° angle. The slope of 45° segment of a Nyquist plot is called the Warburg resistance and is a result of frequency dependence of diffusion of the electrolyte ions into the bulk of the electrode.[15,16] The much shorter Warburg regions of plots for rGO–CNT micro-supercapacitors show the better diffusion of ions into the bulk of electrodes compared to the rGO micro-supercapacitors. Furthermore, the rGO–CNT microdevices show lower equivalent series resistance (ESR) compared to the rGO microdevice (ESR can be calculated from the X-intercepts of Nyquist plots).

For a more informative analysis of EIS tests, the dependence of phase angle with frequency of the microdevices was plotted in Figure 7d. The rGO micro-supercapacitor showed frequency independent phase angles close to –90° for frequencies up to 2 Hz after which the phase angle increased with the increase in frequency. However, the rGO–CNT micro-supercapacitors showed frequency independent phase angle even at frequencies as high as 20 Hz. A better comparison of the frequency response of the microdevices can be made by comparing their characteristic frequency (f_0) which is the frequency at a phase angle of –45° or its corresponding relaxation time constant ($\tau_0 = 1/f_0$). The characteristic frequency marks the point at which the resistive and capacitive impedance are equal and at frequencies higher than f_0 supercapacitor shows a more resistive behavior.[32,33] The corresponding relaxation time constant (τ_0) is the minimum time needed to discharge all the energy from the device with an efficiency of greater than 50%.[10,32] The rGO-CNT-8-2 micro-supercapacitor showed the best frequency response with the characteristic frequency of about 290.7 Hz and time constant of 3.4 ms. The rGO-CNT-9-1 micro-supercapacitor showed a slightly lower time constant of about 4.8 ms (f_0~208.6 Hz). In contrast, the time constant of rGO micro-supercapacitor was about 33 ms. To the best of our knowledge, so far, the best frequency response for a micro-supercapacitor was reported by Pech et al.[10] for OLC micro-supercapacitor tested in 1 M Et_4NBF_4/anhydrous propylene carbonate electrolyte. The OLC micro-supercapacitor, however, showed a time constant of 26 ms and a modest specific capacitance of 1.7 $mFcm^{-2}$ at a CV scan rate of 1 Vs^{-1}, which are both improved in case of our micro-supercapacitors. The volumetric energy and power density of micro-supercapacitors were calculated from CVs at a scan rate of 1 to 50 Vs^{-1} and shown in a Ragone plot (**Figure 8**). It is evident that the drop in energy density with increasing power density is very small in the case of rGO–CNT micro-supercapacitors. At a scan rate of 1 Vs^{-1}, the highest energy density (~0.68 $mWhcm^{-3}$) was recorded for the rGO-CNT-9-1 micro-supercapacitor. This device also shows the highest volumetric power density (~77 Wcm^{-3}) at a scan rate of 50 Vs^{-1}.

The high specific capacitance, exceptional rate capability and high frequency response of the rGO–CNT micro-supercapacitors can be explained by the synergic effects of electrode materials, method of electrode assembly and structural design of micro-supercapacitors. First, using CNT as a nano spacer inhibits the agglomeration and restacking of graphene sheet, thus providing a highly accessible surface area for the microelectrodes. Second, the binder-free deposition based on the ESD technique plays a role in high power handling of the micro-supercapacitors. It is well known that the addition of polymeric binders that are typically used in the fabrication of the electrodes hinders their performance by increasing resistivity and the addition of dead weight.[13,33] Third, another important factor affecting the high power capability of our micro-supercapacitors is the interdigital design of the electrodes. The small distance between the microelectrodes could minimize the electrolyte resistance by reducing the mean ionic diffusion pathway between the microelectrodes. Finally, the small size of the electrodes along with their side by side in-plane design facilitates the diffusion of electrolyte ions between the rGO sheets and in the entire thickness of the electrodes. The rGO–CNT micro-supercapacitors are able to satisfy the power needs of certain miniaturized electronic devices. For instance, they can power radio frequency identification (RFID) tags which generally require 1–100 μW power.[34] Furthermore, the high frequency response of the rGO–CNT micro-supercapacitors makes them an ideal device to be coupled with other devices such as energy harvesters and micro-batteries to provide peak power. With further optimization of the electrode compositions and structural design of micro-supercapacitors, they can potentially meet the necessary requirements to replace low energy and large electrolytic capacitors in ac line-filtering applications in portable electronics.[11] The reported fabrication method of micro-patterned rGO films can also be utilized for the development of other graphene based functional devices.

3. Conclusions

We have demonstrated the development of micro-supercapacitors based on rGO and rGO–CNT patterned microelectrodes with

superior electrochemical properties through the combination of photolithography lift-off and ESD deposition. The fabrication process involved the ESD deposition of electrode materials on masked interdigital current collectors. The GO sheets in the precursor solution were readily reduced to rGO during the low temperature deposition, eliminating the need for further thermal or chemical reduction of GO. In the case of the rGO micro-supercapacitors, the diffusion of electrolyte ions between the rGO sheets resulted in electro-activation of the microelectrodes that increased the average CV current by more than 7 times during the first 200 cycles. We further demonstrated that the addition of CNTs as nano spacers between rGO sheets could minimize their restacking. The electrochemical performance tests indicated that while rGO microdevices had reasonable specific capacitance and power handling ability, the rGO–CNT micro-supercapacitor exhibited exceptional performance. The best results were achieved when a composition of 90% GO and 10% CNT was used in the deposition solution. The stack capacitance of rGO-CNT-9-1 micro-supercapacitors was about 5.0 Fcm^{-3} at a 1 Vs^{-1} CV scan rate, which dropped only by 40% at a very high scan rate of 50 Vs^{-1}. The excellent power response of these micro-supercapacitors was revealed by EIS experiments when an RC time constant of only 4.8 ms was measured at a −45° phase angle, which is lower than any other reported micro-supercapacitors. Increasing the amount of CNTs to 20% slightly improved the power response and rate handling ability of the micro-supercapacitors, but had a negative impact on the specific capacitance. The developed micro-supercapacitors promise high energy micron-scale energy storage units that are able to provide enough energy and satisfy the peak power required for a number of applications. They can also potentially replace low energy electrolytic capacitors in miniaturized electronic devices. We anticipate that further improvement in the performance of micro-supercapacitors can be achieved through the optimization of ESD conditions, microelectrode design, and the composition of the electrode materials.

4. Experimental Section

Preparation of interdigital microelectrodes and removable mask: First, a Ti (20 nm)/Au (300 nm) layer was formed on a Si/(500 nm) SiO_2 by an electron-beam evaporation system. The interdigital current collectors were made by conventional photolithography and wet etching of the Ti/Au layer. To avoid deposition of materials in the space between the microelectrodes and on the contact pads, a removable mask was made on the samples by photolithography. The mask had two layers, a thin (~20 nm) Omnicoat sacrificial bottom layer and a thick (~12 μm) SU-8 (Microchem, USA) top layer. First, the Omnicoat was spin coated on the substrate and was baked at 200 °C for 60 s. Then the SU-8 layer was spin coated, and then baked for 180 s at 65 °C and 300 s at 95 °C. The mask was patterned by photolithography with an OAI 800 mask aligner (OAI, USA) to uncover the microelectrodes. The excess Omnicoat on the uncovered parts of microelectrodes was removed by oxygen plasma treatment at 200 mTorr with a power of 100 W for 30 s.

Preparation of precursor solutions: Single layer GO (6 mg, 0.7–1.2 nm thickness and 300–800 nm dimension, Cheaptubes, Inc., USA) was added to 1,2-propanediol (20 ml, sigma–Aldrich, USA) and dispersed by sonication for 30 min with an ultrasonic probe (750 W, 20 KHz, Sonics and materials Inc., USA) to form a 0.3 $mgml^{-1}$ GO solution. The resultant homogenous solution is stable for several months. This solution was directly used in ESD deposition of rGO samples. In the case of GO-CNT solutions, appropriate amounts of COOH-functionalized multiwalled CNT (8–15 nm diameter and 10-50 μm length Cheaptubes, Inc, USA) was added to the above solution to form solutions with GO:CNT ratios of 9:1 and 8:2, respectively. The solutions were sonicated for 30 min after the addition of CNTs and were immediately used for ESD deposition.

Electrostatic spray deposition: All the samples were deposited by the ESD for 2 h on the masked Ti/Au interdigital microelectrodes. The samples were preheated to 250 °C before the deposition. The prepared precursor solutions were fed to a stainless steel needle using a syringe pump at the rate of 4–5 mlh^{-1}. The distance between the needle and the substrate was kept at 4 cm (Please see Figure S1 for the schematic drawing of the ESD set-up). The solution was sprayed onto the substrate by applying a voltage of 6–7 kV to the needle. After the deposition, the samples were soaked in remover PG (Microchem, USA) to remove the SU8 mask by etching the Omnicoat sacrificial layer.

Characterization of samples: The morphologies of as prepared samples were investigated using a JEOL 7000 field-emission scanning electron microscope (FE-SEM, JEOL, Japan). In order to study the reduction of GO during deposition, FTIR (JASCO FT/IR 4100 spectrometer) was used to analyze the oxygen functionalities of the sample GO before and after deposition. XPS (Physical Electronics 5400 ESCA) was used to quantitatively analyze the chemical compositions of GO and the resulting rGO after the deposition.

Electrochemical testing: After the fabrication of the micro-supercapacitors, the contact pads of each microdevice was connected to aluminum foil using silver paste. Then the microdevices were placed in a homemade Teflon cell with sealed cavity for the electrolyte. After filling the cavity of the cell with 3 M KCL electrolyte, electrochemical studies were performed using a VMP3 multichannel potentiostat (VMP3, Bio-Logic, USA) in the two-electrode mode and at room temperature. CVs were performed at scan rates ranging from 0.01 to 50 Vs^{-1} in a potential range from 0 to 1 V. CD measurements were carried out in the same potential window and with current densities ranging from 3 to 100 $mAcm^{-2}$. EIS measurements were performed at open circuit voltage (OCV) by applying a sinusoidal signal of 10 mV amplitude at frequencies ranging from 100 kHz to 50 mHz. The calculation of specific capacitance and energy and power densities from the above tests are described in the Supporting Information.

Supporting Information

Supporting Information is available from the Wiley Online Library or from the author.

Acknowledgements

The authors would like to thank Advanced Materials Engineering Research Institute at Florida International University. M.B. gratefully acknowledges the financial support from Florida International University, DEA fellowship.

Received: May 12, 2012
Published online: June 29, 2012

[1] M. Beidaghi, W. Chen, C. Wang, *J. Power Sources* **2011**, *196*, 2403.
[2] M.-J. Lee, J. S. Kim, S. H. Choi, J. J. Lee, S. H. Kim, S. H. Jee, Y. S. Yoon, *J. Electroceram.* **2006**, *17*, 643.
[3] M. Xue, Z. Xie, L. Zhang, X. Ma, X. Wu, Y. Guo, W. Song, Z. Li, T. Cao, *Nanoscale* **2011**, *3*, 2703–8.
[4] D. Wei, M. R. J. Scherer, C. Bower, P. Andrew, T. Ryhänen, U. Steiner, *Nano Lett.* **2012**, *12*, 1862.
[5] M. Beidaghi, C. Wang, *Electrochim. Acta* **2011**, *56*, 9508.
[6] K. Wang, W. Zou, B. Quan, A. Yu, H. Wu, P. Jiang, Z. Wei, *Adv. Energy Mater.* **2011**, *1*, 1068–1072.

[7] D. Pech, M. Brunet, P.-L. Taberna, P. Simon, N. Fabre, F. Mesnilgrente, V. Conédéra, H. Durou, *J. Power Sources* **2010**, *195*, 1266.
[8] J. Chmiola, C. Largeot, P. L. Taberna, P. Simon, Y. Gogotsi, *Science* **2010**, *328*, 480.
[9] M. Heon, S. Lofland, J. Applegate, R. Nolte, E. Cortes, J. D. Hettinger, P.-L. Taberna, P. Simon, P. Huang, M. Brunet, Y. Gogotsi, *Energy Environ. Sci.* **2011**, *4*, 135.
[10] D. Pech, M. Brunet, H. Durou, P. Huang, V. Mochalin, Y. Gogotsi, P.-L. Taberna, P. Simon, *Nat. Nanotechnol.* **2010**, *5*, 651.
[11] M. Kaempgen, C. K. Chan, J. Ma, Y. Cui, G. Gruner, *Nano Lett.* **2009**, *9*, 1872.
[12] W. Gao, N. Singh, L. Song, Z. Liu, A. L. M. Reddy, L. Ci, R. Vajtai, Q. Zhang, B. Wei, P. M. Ajayan, *Nat. Nanotechnol.* **2011**, *6*, 6.
[13] J. R. Miller, R. a Outlaw, B. C. Holloway, *Science* **2010**, *329*, 1637.
[14] K. Sheng, Y. Sun, C. Li, W. Yuan, G. Shi, *Sci. Rep.* **2012**, *2*, 247.
[15] M. D. Stoller, S. Park, Y. Zhu, J. An, R. S. Ruoff, *Nano Lett.* **2008**, *8*, 3498.
[16] Y. Wang, Z. Shi, Y. Huang, Y. Ma, C. Wang, M. Chen, Y. Chen, *J. Phys. Chem. C* **2009**, *113*, 13103.
[17] Y. Zhu, S. Murali, M. D. Stoller, K. J. Ganesh, W. Cai, P. J. Ferreira, A. Pirkle, R. M. Wallace, K. a Cychosz, M. Thommes, D. Su, E. A. Stach, R. S. Ruoff, *Science* **2011**, *332*, 1537.
[18] Q. Cheng, J. Tang, J. Ma, H. Zhang, N. Shinya, L.-C. Qin, *Phys. Chem. Chem. Phys.* **2011**, *13*, 17615.
[19] Y. Wang, Y. Wu, Y. Huang, F. Zhang, X. Yang, Y. Ma, Y. Chen, *J. Phys. Chem. C* **2011**, *115*, 23192.
[20] S.-Y. Yang, K.-H. Chang, H.-W. Tien, Y.-F. Lee, S.-M. Li, Y.-S. Wang, J.-Y. Wang, C.-C. M. Ma, C.-C. Hu, *J. Mater. Chem.* **2011**, *21*, 2374.
[21] J. J. Yoo, K. Balakrishnan, J. Huang, V. Meunier, B. G. Sumpter, A. Srivastava, M. Conway, A. L. M. Reddy, J. Yu, R. Vajtai, P. M. Ajayan, *Nano Lett.* **2011**, *11*, 1423.
[22] C. D. Zangmeister, *Chem. Mater.* **2010**, *22*, 5625.
[23] H. C. Huang, C. W. Huang, C. T. Hsieh, P. L. Kuo, J. M. Ting, H. Teng, *J. Phys. Chem. C* **2011**, *115*, 20689.
[24] W. Gao, L. B. Alemany, L. Ci, P. M. Ajayan, *Nat. Chem.* **2009**, *1*, 403.
[25] B. Xu, S. Yue, Z. Sui, X. Zhang, S. Hou, G. Cao, Y. Yang, *Energy Environ. Sci.* **2011**, *4*, 2826.
[26] X. Fan, W. Peng, Y. Li, X. Li, S. Wang, G. Zhang, F. Zhang, *Adv. Mater.* **2008**, *20*, 4490.
[27] O. C. Compton, B. Jain, D. a Dikin, A. Abouimrane, K. Amine, S. T. Nguyen, *ACS Nano* **2011**, *5*, 4380.
[28] Y. Gogotsi, P. Simon, *Science* **2011**, *334*, 917.
[29] H. J. In, S. Kumar, Y. Shao-Horn, G. Barbastathis, *Appl. Phys. Lett.* **2006**, *88*, 083104.
[30] Z. Weng, Y. Su, F. Li, J. Du, *Adv. Energy Mater.* **2011**, *1*, 917.
[31] G. Wang, L. Zhang, J. Zhang, *Chem. Soc. Rev.* **2011**, *41*, 797.
[32] P. L. Taberna, P. Simon, J. F. Fauvarque, *J. Electrochem. Soc.* **2003**, *150*, A292.
[33] V. Presser, L. Zhang, J. J. Niu, J. McDonough, C. Perez, H. Fong, Y. Gogotsi, *Adv. Energy Mater.* **2011**, *1*, 423.
[34] J. A. Paradiso, *IEEE Pervasive Comput.* **2005**, *4*, 18.